Minimal geometric requirements for micropropulsion via magnetic rotation

U Kei Cheang,[1] Farshad Meshkati,[2] Dalhyung Kim,[1,3] Min Jun Kim,[1,*] and Henry Chien Fu[2,†]
[1]*Department of Mechanical Engineering and Mechanics, Drexel University, Philadelphia, Pennsylvania 19104, USA*
[2]*Department of Mechanical Engineering, University of Nevada, Reno, Reno, Nevada 89557, USA*
[3]*The Rowland Institute, Harvard University, Cambridge, Massachusetts 02142, USA*
(Received 29 May 2014; published 12 September 2014)

Controllable propulsion of microscale and nanoscale devices enhanced with additional functionality would enable the realization of miniaturized robotic swimmers applicable to transport and assembly, actuators, and drug delivery systems. Following biological examples, existing magnetically actuated microswimmers have been designed to use flexibility or chirality, presenting fabrication challenges. Here we show that, contrary to biomimetic expectations, magnetically actuated geometries with neither flexibility nor chirality can produce propulsion, through both experimental demonstration and a theoretical analysis, which elucidates the fundamental constraints on micropropulsion via magnetetic rotation. Our results advance existing paradigms of low-Reynolds-number propulsion, possibly enabling simpler fabrication and design of microswimmers and nanoswimmers.

DOI: 10.1103/PhysRevE.90.033007 PACS number(s): 47.61.−k, 47.63.Gd, 47.63.M−, 87.85.gf

Nanoscale and microscale swimming robots have been intensely investigated due to their many possible applications, including micromanipulation and microfabrication [1,2], drug delivery [3,4], tissue manipulation [2,5], and *in situ* sensing [6], such as *in vivo* diagnostics [7–9]. However, difficulties in developing effective propulsion systems have limited their development. Microscale propulsion has been achieved using electrically and optically controlled bacteria [10], magnetically steered swimming cells [11], optically deformed three-bead systems [12], biflagellate micro-objects [13], and chemically driven phoretic robots [14–22]. Here we focus on another broad class of robotic microswimmers, those actuated by rotating magnetic fields. Swimming at microscales and below vastly differs from macroscales since viscous damping dominates inertial forces, implying that the hydrodynamics are governed by the zero-Reynolds-number Stokes equation.

Some magnetically actuated microswimmers and nanoswimmers, such as colloidal walkers [23], rotors [24], nanowires [25], and drillers [26] rely on nearby surfaces for propulsion, which limits their range of applicability. Away from surfaces, in bulk fluids current efforts to make robotic microswimmers have followed biological examples that use either chirality or flexibility to achieve nonreciprocal swimming strokes (i.e., strokes that do not trace the same sequence of configurations forward and backward in time), as required for force- and torque-free biological swimmers by the Scallop theorem [27]. The archetypal chiral strategy is the bacterial flagellum, which is a nearly rigid helix rotating relative to the cell body [28]. The rotating flagellum forms a helical traveling wave so it is not a reciprocal motion. Various artificial helical swimmers [29–35] have achieved controlled propulsion under magnetic rotation. The archetypal flexible strategy is the sperm flagellum. Nonreciprocal traveling waves propagate down the flexible flagellum to produce propulsion even for in-plane (hence achiral) beating patterns [36]. Flexible artificial swimmers include spermlike swimmers fabricated by DNA linkage [36] and nanowire robots [37,38]. Based on these biomimetic expectations, challenging fabrication techniques have been required to create chiral or flexible structures.

Here, we show that neither chirality nor flexibility is necessary for propulsion of robotic microswimmers actuated by external rotating magnetic fields away from surfaces. We demonstrate experimentally that an achiral, rigid colloidal microswimmer constructed of three magnetic beads is capable of externally actuated locomotion and is easily maneuvered. We present a theoretical analysis that elucidates the criteria that apply for rigid microswimmers rotated by external torque, establishing fundamental guidelines for designing such microswimmers and nanoswimmers, which may lead to simpler fabrication of magnetic microswimmers than currently used.

I. METHODS

A. Fabrication of achiral microswimmers

We fabricated achiral microswimmers using three ferromagnetic microparticles (4.40 μm in diameter) linked together, forming the simplest structure for a microswimmer. Naturally, dipole interactions tend to self-assemble the magnetic particles linearly, but we need to make a bent geometry. Chemical streptavidin-biotin binding was used to overcome the linearity of the magnetic self-assembly to form the curved structures necessary for swimming.

The swimmers contain two types of particles. Both of those particles possess the same magnetic properties and are of the same size (4.40 μm). The difference between the two types of beads is the surface coating: one with streptavidin, and the other with biotin. The two are diluted using 30 mg/mL NaCl solution to 0.1 mg/mL and then combined in a reaction mix to make the three-bead microswimmers. The dilution was used to avoid aggregation and increase the probability to create three-bead swimmers. This mixing method introduces randomness to the fabrication process; nonetheless, three-bead structures can be obtained in this process. Another concern is the rigidity of the swimmers. Some three-bead structures are prone to deformation while under a magnetic field, while others are relatively rigid. As detailed in Sec. II A, only swimmers that

*mkim@coe.drexel.edu
†hfu@unr.edu

have a rigid structure were used for experiments. The binding affiliation between streptavidin and biotin is the strongest among naturally found noncovalent bonds [39,40], so the swimmers will be relatively unbreakable and rigid [41] while under strong magnetic forces during experiments.

B. Magnetic control of swimmers far from surfaces

To generate the rotating magnetic field which actuates the achiral microswimmers, we used a control system consisting of three pairs of electromagnetic coils arranged in an approximate Helmholtz configuration (see Appendix), three Kepco power supplies (BOP 20-5M), a National Instruments data acquisition (DAQ) system, a computer, an inverted microscope (Leica DM IRB), and a high-speed camera (FASTCAM SA3). Through the use of a DAQ system, the power supplies generate sinusoidal outputs to the coils to create a rotating magnetic field. The high-speed camera provides visual feedback and records videos at high frame rates (60–100 fps). The computer is used as interface for the camera and the DAQ system. The three pairs of coils are designed to exert torque on the swimmer without introducing translational force by creating a spatially uniform magnetic field with any specified time-dependent magnitude and direction in a 2 mm × 2 mm × 2 mm region. Experiments take place with swimmers immersed in 0.3 g/mL NaCl solution (viscosity of 1 mPa s) in a 3 mm × 3 mm × 2 mm (L × W × H) polydimethylsiloxane (PDMS) chamber, sealed to minimize fluid flow and evaporation, and placed at the center of the approximate Helmholtz coil system mounted on the microscope. The concentration of the NaCl solution was chosen to minimize vertical drift from sedimentation or buoyancy, indicating that the swimmers have density less than 1.2 g/mL. A video is provided showing a swimmer located far from a boundary [42]. At this and higher concentrations, we observed some beads rising due to buoyancy. Out of many imaged videos, we analyzed those where the vertical drift from sedimentation or buoyancy was smallest, so that the swimmer could be kept in the plane of focus. The focal plane was always at least 20 μm from the chamber surfaces. As described later, we also insured that boundary effects were negligible by observing the direction of swimming motion relative to the magnetic field rotation axis: boundary effects make swimmers roll along the surface in a direction perpendicular to the rotation axis, while bulk swimmers move in a direction along the rotation axis [43].

C. Three-dimensional image processing and analysis

Changes in structure, swimmer rotation, and swimmer translation are quantified using a three-dimensional (3D) tracking algorithm written in MATLAB. Since the structure of the swimmer consists of three spherical beads, the algorithm tracks the three Cartesian positions (x,y,z) of each bead. Planar positions (x,y) are obtained from the centroid of the bead images. Vertical positions (z) are obtained from a standard-deviation-based algorithm that detects the changes in intensity of the beads which correspond to changes in the distance from the focal plane (see autofocusing algorithms reviewed by Sun *et al.* [44]).

II. CONTROLLED ACHIRAL RIGID MICROSWIMMERS

We fabricated an achiral microswimmer consisting of three ferromagnetic spherical beads (4.40 μm average diameter) linked together, which forms a simple structure for a swimmer [Fig. 1(a)]. Dipole interactions tend to lead to linear self-assembly of the magnetic particles, so streptavidin-biotin binding [39,40] was used to stabilize randomly formed bent nonlinear structures necessary for swimming. Since the centers of the three beads define a plane of mirror symmetry (even for beads of different diameters), the structure is achiral. After assembly, the swimmer has a magnetic dipole, which allows us to manipulate its orientation by applying a spatially uniform, time-dependent magnetic field. The swimmers are

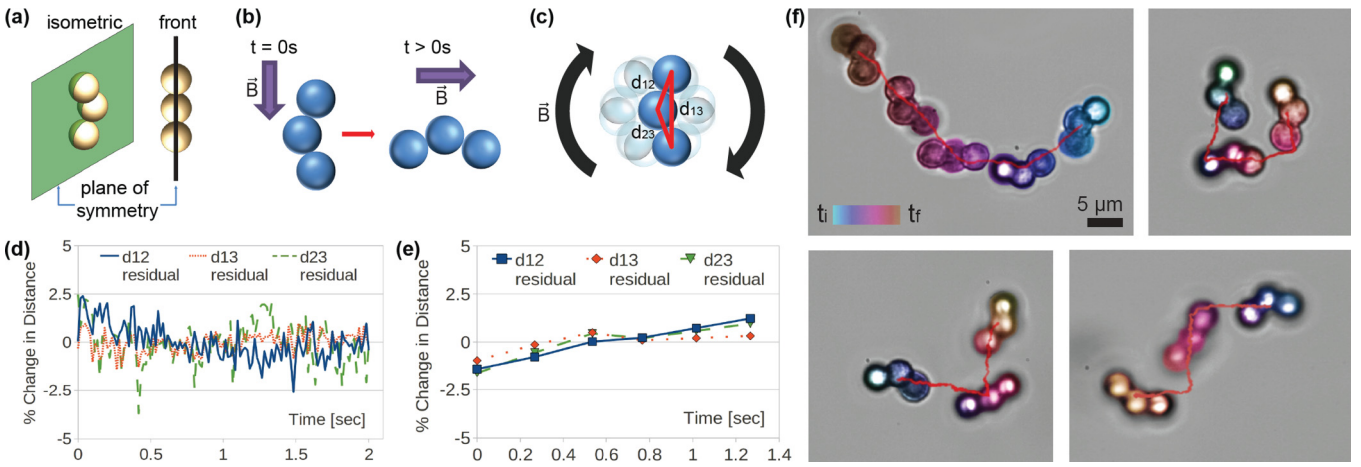

FIG. 1. (Color online) Controlled achiral rigid microswimmers. (a) The microswimmers' three-bead structure contains a plane of symmetry making it achiral. (b), (c) Schematic of flexibility tests to quantify microswimmers rigidity under (b) impulsive reorientation and (c) steady rotation. The microswimmer's structure is measured by the three-dimensional distances between each pair of beads (d_{12}, d_{23}, d_{13}). (d) Percentage change in (d_{12}, d_{23}, d_{13}) during impulsive reorientation. (e) Percentage change in (d_{12}, d_{23}, d_{13}) during swimming with data points captured once per cycle when the swimmer is nearly perpendicular to the line of sight. In (d) and (e) distances change less than 5% indicating rigid geometry. (f) Trajectories of achiral microswimmers showing swimmers controlled to swim in different patterns and make sharp turns.

large enough that Brownian motion is negligible compared to observed swimming velocities [45].

A. Rigidity of swimmers

Due to the randomness in the fabrication process, not all microswimmers were rigid. The results reported are for those which do not deform by visual inspection. We further quantified the rigidity of these swimmers by observing their response to time-dependent magnetic fields (Figs. 1(b) and 1(c) and Supplemental video [42]). First, to determine whether the swimmer elastically deforms in response to torque, its geometry was observed while it reoriented in response to a time-dependent magnetic field. Swimmers were first allowed to come to equilibrium in a static field, with dipole moment aligned with the field. Then the static field was changed instantaneously to a direction perpendicular to the original direction while maintaining the same magnitude [Fig. 1(b)]. This sequence imposes a sudden torque on the swimmer, which relaxes as the swimmer reorients to align its moment with the field. During the reorientation, we tracked the distances between the three beads [d_{12}, d_{23}, d_{13}, Figs. 1(b) and 1(c)] in three dimensions. Second, to determine whether the swimmer irreversibly deforms under the torques exerted by rotating fields, we investigated the change in swimmer geometry while it was rotated continuously (as might occur during swimming) about the x axis [Fig. 1(c)]. In this and our swimming experiments, the magnetic field is perpendicular to its rotation axis. We tracked the distance between beads over six periods of rotation (1.5 seconds), a time comparable to those used to measure swimming velocities. To minimize error in the z displacements, we measure the distances once per rotation, when the swimmer plane is oriented nearly perpendicularly to the line of sight. Representative results from the rigidity tests for a visually rigid swimmer are shown in Figs. 1(d) and 1(e). The lengths d_{12}, d_{23}, and d_{13} change by less than 5%.

The observed <5% deformations are not responsible for the propulsion, since as detailed in Sec. III our theoretical model shows that rigid swimmers of similar geometries are capable of propulsion, and the model estimates swimming speeds of the same order of magnitude as those observed.

B. Swimming and motion control

We observe that the direction of the average velocity is along the rotation axis of the field. The swimmer rotates along a body-fixed axis as it swims. Altering either the angular velocity or magnitude of the applied rotating magnetic field alters the body-fixed rotation axis and the velocity of the swimmer. In contrast, swimmers relying on boundary effects roll in a direction perpendicular to the rotation axis of the field [43], and we use this fact to ensure that the swimmers we observe are not affected by a boundary.

To validate swimming capability and controllability of the achiral swimmer, we changed the strength, direction, and frequency of the rotating magnetic field. The swimming direction can be controlled by manipulating the direction of the magnetic fields rotational axis. To control motion in the xy plane we use the approximate Helmholtz coil system to apply a time-dependent magnetic field $\mathbf{B} = B_i[\sin\theta\sin(\omega t+\phi)\hat{\mathbf{i}} + \cos\theta\sin(\omega t+\phi)\hat{\mathbf{j}} + \sin\omega t\hat{\mathbf{k}}]$ that rotates with angular velocity $\boldsymbol{\omega} = \omega(-\cos\theta\hat{\mathbf{i}} + \sin\theta\hat{\mathbf{j}})$ (which is the average swimming direction). The phase ϕ is either -90° or 90°. By changing θ the achiral swimmer could make sharp turns at any angle (see SM video). Figure 1(f) and the Supplemental video [42] show several swimming trajectories illustrating directional control. For these trajectories, the rotational frequency and field strength were kept constant, maintaining constant swimming speed. In addition, turning the field on and off or reversing the rotation resulted in starting and stopping motion or direction reversal, respectively.

III. GEOMETRICAL REQUIREMENTS FOR SWIMMING

The swimmer described above demonstrates the ability to convert external rotational torque to translational motion without a chiral or flexible geometry. Here we analyze the coupled rotational and translational motion of the achiral swimmer working in a frame fixed relative to the body of the swimmer (principal axes of rotation $\mathbf{e}_1$, $\mathbf{e}_2$, $\mathbf{e}_3$ in Fig. 2; $\mathbf{e}_2$ and $\mathbf{e}_3$ are perpendicular to the symmetry planes of the swimmer), and show that such motion is consistent with the principles of low-Reynolds number hydrodynamics.

In the Stokes regime, the translational velocity $\mathbf{v}$ and angular velocity $\boldsymbol{\Omega}$ are related to the force $\mathbf{F}$ and torque $\mathbf{N}$ on the swimmer by the 6×6 mobility matrix [46]:

$$\begin{pmatrix}\mathbf{v}\\ \boldsymbol{\Omega}\end{pmatrix} = \begin{pmatrix}\mathbf{K} & \mathbf{C}\\ \mathbf{C}^{\mathsf{T}} & \mathbf{M}\end{pmatrix}\begin{pmatrix}\mathbf{F}\\ \mathbf{N}\end{pmatrix}, \tag{1}$$

where the 3×3 submatrices $\mathbf{K}$, $\mathbf{M}$, and $\mathbf{C}$ relate the translational velocity and force, rotational velocity and torque, and translational velocity and torque, respectively.

For a swimmer with permanent magnetic dipole $\mathbf{m}$, the torque $\mathbf{N}$ on the swimmer due to the external field is $\mathbf{N} = \mathbf{m}\times\mathbf{H}$, where $\mathbf{H}$ is the magnetic field, and for the uniform fields in the experiment there is no net external force. Therefore

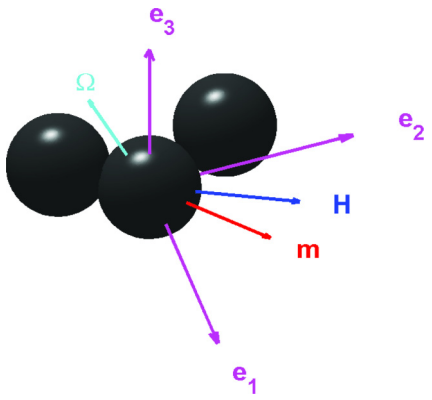

FIG. 2. (Color online) Schematic for analyzing swimmer dynamics in body-fixed frame. $\mathbf{e}_1$, $\mathbf{e}_2$, and $\mathbf{e}_3$ are the principal axes of $\mathbf{M}$; $\mathbf{e}_2$ and $\mathbf{e}_3$ are perpendicular to the symmetry planes of the swimmer. For steady rotation, the swimmer angular velocity $\boldsymbol{\Omega}$ coincides with the magnetic field rotation, and the magnetic field $\mathbf{H}$ and its angular velocity are constant in the body-fixed frame. The magnetic field is perpendicular to its angular velocity.

the instantaneous angular velocity is

$$\mathbf{\Omega} = \mathbf{M}(\mathbf{m} \times \mathbf{H}). \tag{2}$$

In general, as the swimmer and the external field rotate independently, the orientation of $\mathbf{H}$ changes relative to the body-fixed frame. However, a steady-state solution arises if the swimmer angular velocity $\mathbf{\Omega}$ is equal (in magnitude and direction) to the magnetic field rotation $\boldsymbol{\omega}$.

Now assume that rotational dynamics are in steady state, as is the case when the swimmers are observed to rotate with the field. Then the translational velocity produced by the external torque is

$$\mathbf{v} = \mathbf{C}(\mathbf{m} \times \mathbf{H}), \tag{3}$$

which like the angular velocity is time independent in the body-fixed frame. Generically, an object with constant body-fixed $\mathbf{v}$ and $\mathbf{\Omega}$ moves in circular or helical trajectories [47]. A net translational swimming velocity requires a helical trajectory, for which $\mathbf{v} \cdot \Omega \neq 0$. Thus, the minimal criteria for swimming are that the swimmer rotation $\mathbf{\Omega}$ [Eq. (2)] is equal to the field rotation $\boldsymbol{\omega}$, and $\mathbf{\Omega} \cdot [\mathbf{C}(\mathbf{m} \times \mathbf{H})] \neq 0$.

A necessary condition for swimming is that $\mathbf{C}$ is nonzero. Based on standard symmetry analyses [46], geometries with axisymmetry or three perpendicular mirror planes of symmetry have $\mathbf{C} = 0$ and no swimming, but geometries with up to two perpendicular mirror planes of symmetry can have nonzero $\mathbf{C}$ and produce swimming. In particular, swimming is possible for rigid, achiral geometries. To be concrete, consider a swimmer composed of three equally sized beads such as those fabricated for our experiments [Fig. 1(a)]. For this geometry, symmetry analysis reveals that $\mathbf{M}$ and $\mathbf{C}$ take the form [46]

$$\mathbf{M} = \begin{pmatrix} M_1 & 0 & 0 \\ 0 & M_2 & 0 \\ 0 & 0 & M_3 \end{pmatrix}; \qquad \mathbf{C} = \begin{pmatrix} 0 & 0 & 0 \\ 0 & 0 & C_{23} \\ 0 & C_{32} & 0 \end{pmatrix} \tag{4}$$

referred to the body-fixed axes labeled $\mathbf{e}_1, \mathbf{e}_2, \mathbf{e}_3$ in Fig. 2 [48]. We also verified the form of the mobility matrix by explicit calculation for rigid bodies composed of beads of diameter 4.40 μm using the method of regularized Stokeslets [47,49,50] (see Appendix for details).

Substituting these mobility matrices into Eqs. (2) and (3) shows that for this achiral swimmer, the torque must have both $\hat{\mathbf{e}}_2$ and $\hat{\mathbf{e}}_3$ components in order for swimming to be possible. This implies that $\mathbf{m}$ cannot lie along either the 2 or 3 directions, which are the directions perpendicular to the symmetry planes of the swimmer. Solving Eqs. (2) and (3) explicitly for a geometry corresponding to our achiral three-bead swimmers confirms that under external rotating torques, such geometries swim with the order 1 μm/s speeds observed in our experiments (see Appendix for details).

Note that the propulsion of our swimmers is consistent with the Scallop theorem and kinematic reversibility of the Stokes equations: as a rigid body, our swimmers do not undergo swimming deformations and instead are actuated by a nonreciprocal external torque. Here we point out that the chirality employed in previous examples of rigid magnetically rotated swimmers is not necessary to have nonzero $\mathbf{C}$ and hence swimming.

If a steady solution to Eq. (2) exists ($\mathbf{\Omega} = \boldsymbol{\omega}$), it depends on both the frequency of rotation and the strength of the magnetic field. An important timescale of the rotational dynamics is the typical timescale for rotation of the swimmer due to an external field of magnitude $|\mathbf{H}|$, which is determined by balancing viscous rotational drag against the external torque. From Eq. (2), the timescale is given by $T_{\text{viscous}} = (||\mathbf{M}||\mathbf{m}||\mathbf{H}|)^{-1}$, where $||\mathbf{M}||$ is the typical magnitude of rotational mobility of the particle. If T_{viscous} is short compared to the timescale of variation of the magnetic field ($T_B = 2\pi/\omega$), then the swimmer is in a quasistatic regime, with its magnetic dipole always nearly aligned with the external field. If T_{viscous} is much longer than T_B, then the swimmer cannot rotate quickly enough to follow the magnetic field, and the swimmer will not rotate steadily. For steady-state solutions in the intermediate regime the dipole is not aligned with the external field, producing enhanced torques, hence the rotation axis of the swimmer varies.

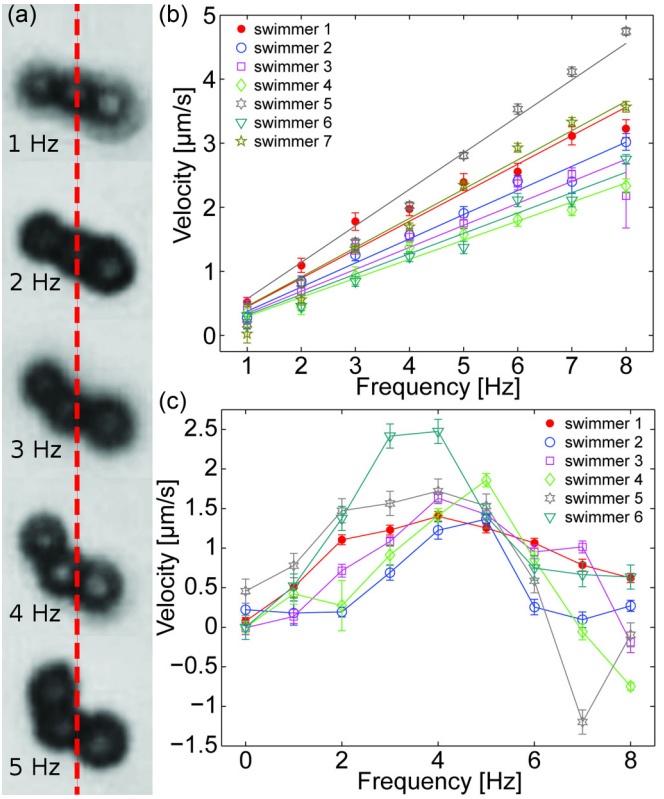

FIG. 3. (Color online) Response of swimmer to rotation frequency. (a) The rotational axis (demarcated by red dashed line) changes relative to swimmer's orientation as rotation frequency changes with constant field strength. The swimmer's rotation transitions from a symmetrical axis (low frequencies) to a non-symmetrical axis (high frequencies). (b) Swimming speed of seven different achiral microswimmers as frequency and field strength are varied with their ratio held constant. Equation (2) predicts a linear relation; linear fit data and ratio of frequency to field strength are reported in Table I. Due to the random fabrication process, each swimmer has a different geometry hence different swimming speed. (c) Swimming speed of the six different microswimmers as frequency is varied for constant field strength, including the microswimmer in (a) shown as swimmer 6. Error bars in (b) and (c) denote standard errors estimated from position uncertainty in image analysis and observation time used to measure velocity.

TABLE I. Linear regression values for the seven microswimmers in Fig. 3(b).

swimmer	1	2	3	4	5	6	7
Slope (μm s^{-1}mT^{-1})	0.4454	0.3770	0.3435	0.2972	0.6614	0.4567	0.3492
R^2	0.9309	0.9799	0.8567	0.9745	0.9989	0.9662	0.9729
f/H (Hz/mT)	0.551	0.734	0.734	0.743	3.67	5.51	5.51

IV. QUALITATIVE PREDICTIONS AND EXPERIMENTS

To satisfy Eq. (2) for a given ω, the magnetic field $\mathbf{H}$ and its rotation vector $\boldsymbol{\omega}$ must take specific orientations relative to the swimmer, which varies as ω varies. Since $\boldsymbol{\Omega} = \boldsymbol{\omega}$, the direction of $\boldsymbol{\omega}$ also sets the swimmers rotation axis as well as the direction of average swimming translation. Frequency dependent rotational axes have also been observed and modeled for magnetically actuated swimmers and gyroscopes both in bulk fluids and near surfaces [26,43,51–53]. Together, these considerations make qualitative predictions that can be checked experimentally.

First, no swimming results if the torque is perpendicular to one of the planes of mirror symmetry (i.e., along $\mathbf{e}_2$ and $\mathbf{e}_3$) or along $\mathbf{e}_1$, in which case the rotational axis is also along $\mathbf{e}_1$, $\mathbf{e}_2$, or $\mathbf{e}_3$. In our experiments we indeed observe that the swimmers' rotation axes change as we change the rotation frequency [representative result in Fig. 3(a)] and that the swimmers only swim when they rotate around an axis which is not $\mathbf{e}_1$, $\mathbf{e}_2$, or $\mathbf{e}_3$.

Second, examination of Eq. (2) shows that constant rotation and field directions satisfy Eq. (2) if the rotation frequency and magnetic field strength are increased proportionally. In that case, Eq. (3) implies the swimming speed increases linearly with the frequency. This linear relationship was observed experimentally [Fig. 3(b)]. We tracked seven different swimmers while the frequency and magnetic field strength were increased proportionally [Fig. 3(b)]. During the experiments, the swimmers were all controlled to swim in the positive x direction. For swimmers 1–7, the velocity-frequency data had linear fits through the origin with R^2 ranging from 0.8567–0.99894 (Table I). The linear relation was confirmed for a variety of frequency-to-magnetic field strength ratios (Table I). Since our fabrication process results in random geometries, each swimmer has a different geometry and hence a different swimming speed. Nonetheless, all demonstrate the linear relationship predicted by our theory.

Third, if the frequency is increased while the magnetic field strength is held constant, the swimmer body-fixed rotation axis changes, leading to a complicated nonlinear dependence of swimming speed on frequency. A Supplemental video shows this behavior for one swimmer [42]. In Fig. 3(c), we show the swimming speed for six microswimmers as a function of frequency while magnetic field strength is held constant. In contrast to Fig. 3(b), the relationship between swimming speed and frequency is nonlinear and markedly nonmonotonic. Note that our analysis assumed a permanent dipole, which approximates the magnetic moment of a soft ferromagnet under saturating fields when the direction of the magnetic field is fixed relative to the swimmer body. In the experimental case, the direction of the field changes as the rotation axis changes. Therefore some of the nonlinearity in Fig. 3(b) results from changes in the moment as the rotation axis changes under frequency. However, the changes in rotation axis play a key role in driving the nonlinearity in the context of our analysis, as can be seen from the behavior of the swimmer shown in Fig. 3(a) [corresponding to swimmer 6 in Fig. 3(c)]. For frequencies less than or equal to 2 Hz, the swimmer rotates near axis $\mathbf{e}_1$, and accordingly the swimming velocities are small. Between 3 Hz and 5 Hz, the swimmer rotates around non-principal axes, and there is appreciable propulsion. At 6 Hz, the swimmer rotates near axis $\mathbf{e}_2$, and the swimming velocity is small again. Above 7 Hz, the swimmer does not rotate steadily in synchrony with the magnetic field, hence 7 Hz is the step-out frequency.

V. DISCUSSION

Previous work on robotic microswimmers focused on flexible or chiral structures to generate propulsion; here, our achiral microswimmers have shown that neither is necessary. Our analysis of the achiral microswimmer provides a framework to describe the coupled rotational and translational motion of magnetically rotated microswimmers of arbitrary geometries, as well as the minimal criteria for propulsion of rigid bodies under external torque. Applying this framework to design artificial microswimmers without chirality may lead to simpler fabrication methods than currently used for helical or flexible microswimmers and nanoswimmers, advancing their development for numerous applications. Although the particular swimmers demonstrated here are not faster than previously fabricated microrobots, our work expands the space of geometries to be considered for optimization of swimming performance, thus opening possibilities for more effective propulsion as well.

ACKNOWLEDGMENTS

We thank Hoyeon Kim for help in system setup. This work was funded by National Science Foundation (CMMI 1000255) and Army Research Office (W911NF-11-1-0490) awards to M.K., by National Science Foundation awards (CBET-1067798, CBET-0967510, and DMR-1307497) to H.F., and by a National Science Foundation Graduate Research Fellowship (NSF-GRF) awarded to U.C.

APPENDIX A: MAGNETIC FIELD PRODUCED BY APPROXIMATE HELMHOLTZ COILS

The approximate Helmholtz coils in this study are arranged in a slightly different configuration than that of a normal Helmholtz coil. Conventionally, the distance between two coils of the same size is the radius of the coils, which creates a near-constant magnetic field in the central region between the coils. In this study, the distance between each pair of coils

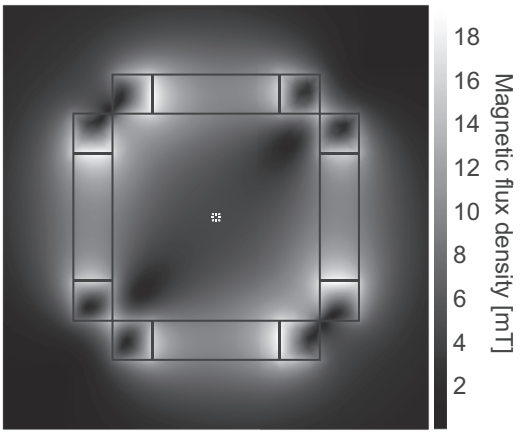

FIG. 4. Modeled magnetic field. Density plot of magnetic field in xy plane created by the coil system modeled using COMSOL MULTIPHYSICS. The small box at the center shows the area where the magnetic field is near uniform (<2% variation).

is equal to the outer diameter of the coils plus the thickness for the coil, which allows a cubelike configuration for the 3D coil system and fits within the geometrical constraints of the microscope while maintaining the desired characteristics of the Helmholtz configuration. In order to validate the magnetic field strength as well as the field profile, a finite element method was used to model the coil system in COMSOL MULTIPHYSICS. The finite element model simulated the magnetic field using two pairs of coils producing a magnetic field with x and y components, generating a static magnetic field in the xy plane. The approximate Helmholtz coil system produces a near-constant magnetic field at the center region of the coil system within which the magnetic flux has less than 2% variation; this region is indicated in Fig. 4 by the red box marking an area approximately 2 mm by 2 mm. The magnetic field strength (mT), rotational direction of the magnetic field, and rotational frequency (Hz) of the field generated by the coils are controlled through LABVIEW. The simulation indicates a field strength of 5.06 mT when a current of 1 A passes through the coils, which matches the experimentally measured value of approximately 5 mT. According to the Biot-Savart law, the field strength scales linearly with the applied current; this is also validated with the simulated model and experimental measurements.

APPENDIX B: EXPLICIT CALCULATION OF MOBILITY MATRIX

To verify the results for the symmetry analysis of the submatrix $\mathbf{C}$ of the mobility matrix, we numerically calculate the mobility matrix for rigid bodies composed of three beads by using the method of regularized Stokeslets [47,49,50]. The surface discretization used 717 regularized Stokeslets [Fig. 5(a)]. To find the mobility matrix, we calculate the force and torque on the swimmer for prescribed rigid-body translations in each of the cartesian directions and for prescribed rigid-body rotations along each of the cartesian directions. This yields the resistance matrix, which is the inverse of the mobility matrix.

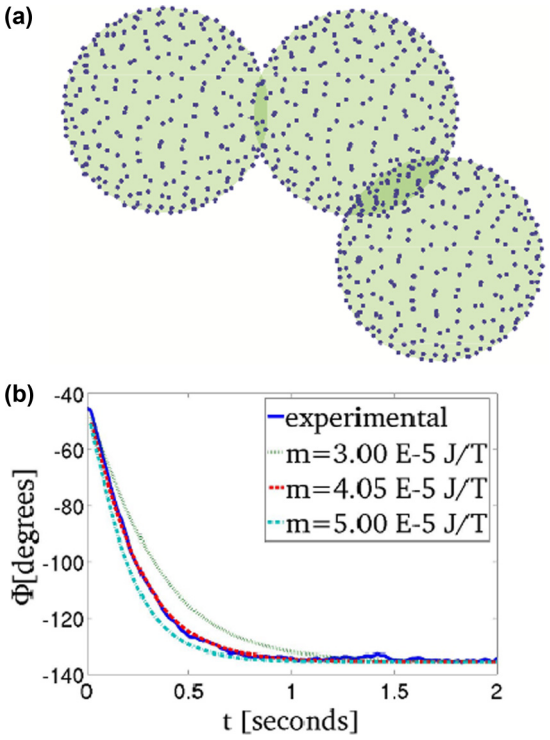

FIG. 5. (Color online) (a) Schematic of discretized surface of the swimmer. Each of the 717 points represents a regularized Stokeslet on the surface of the swimmer. (b) Angular reorientation of the swimmer during the reorientation test (solid blue line), along with simulated angular reorientation for different magnitudes of the magnetic dipole (green dotted, red dashed, turquoise dash-dotted lines). The best fit corresponds to a moment of 4.05×10^{-15} J/T.

We calculate $\mathbf{C}$ for two cases. First, we consider the fully symmetric case with three beads of radius 4.40 μm, with centroids of the beads located 8.80 μm apart, which has two perpendicular planes of mirror symmetry. We verified that when the origin is taken to be the center of reaction, the form agrees with that of the symmetry analysis [Eq. (4)] up to machine precision.

Second, because irregularities during fabrication can produce less symmetric three-bead swimmers, we also calculate $\mathbf{C}$ for three beads of different sizes or with different lengths between their centroids, which produces structures with only a single plane of mirror symmetry, the plane containing the centroid of the three beads. In that case, the symmetry analysis of Happel and Brenner [46] implies that $\mathbf{C}$ takes the form

$$\mathbf{C} = \begin{pmatrix} 0 & 0 & C_{13} \\ 0 & 0 & C_{23} \\ C_{31} & C_{32} & 0 \end{pmatrix}. \tag{B1}$$

Again, the numerically calculated mobility matrices for these less symmetric geometries, including geometries deduced from experimental image analysis, have the form predicted by symmetry analysis.

APPENDIX C: CALCULATED SWIMMING SPEEDS

We used the mobility matrices to calculate the swimming speed for a 10.12 mT magnetic field rotating at 4 Hz by solving Eqs. (2) and (3) numerically. The calculation requires a measurement of the magnetic dipole. The random fabrication process means that each swimmer has a different dipole magnitude and direction, but to obtain an estimate of swimming speeds, we estimated the moment via the response of a single swimmer to the reorientation experiment used to test rigidity [Fig. 1(b)]. The magnetic field strength in this experiment was 2.53 mT. The direction of the magnetic moment was determined from the initial and final orientations of the swimmer. The magnitude of the moment was obtained by modeling the rotation dynamics using Eq. (2) and the mobility matrix calculated above. We found that a moment of 4.05×10^{-15} J/T provided the best fit to the reorientation dynamics, as measured by the sum of squared residuals [Fig. 5(b)]. For this magnitude of dipole moment in a variety of directions, and a variety of three-bead swimmer geometries, we found that swimming speeds had typical orders of magnitude of 1 μm/s.

[1] A. Ferreira, J. Agnus, N. Chaillet, and J. M. Breguet, Mechatronics, IEEE/ASME Transactions on **9**, 508 (2004).

[2] H. Zhang, D. W. Hutmacher, F. Chollet, A. N. Poo, and E. Burdet, Macromol. Biosci. **5**, 477 (2005).

[3] G. Dogangil, O. Ergeneman, J. Abbott, S. Pane, H. Hall, S. Muntwyler, and B. Nelson, in *IEEE/RSJ International Conference on Intelligent Robots and Systems, 2008* (IEEE, New York, 2008), pp. 1921–1926.

[4] S. Fusco, G. Chatzipirpiridis, K. M. Sivaraman, O. Ergeneman, B. J. Nelson, and S. Pan, Adv. Healthcare Mater. **2**, 1037 (2013).

[5] S. Kim, F. Qiu, S. Kim, A. Ghanbari, C. Moon, L. Zhang, B. J. Nelson, and H. Choi, Adv. Mater. **25**, 5863 (2013).

[6] X. Liu, K. Kim, Y. Zhang, and Y. Sun, Int. J. Robot. Res. **28**, 1065 (2009).

[7] S. Martel, J.-B. Mathieu, O. Felfoul, A. Chanu, E. Aboussouan, S. Tamaz, P. Pouponneau, L. Yahia, G. Beaudoin, G. Soulez, and M. Mankiewicz, Appl. Phys. Lett. **90**, 114105 (2007).

[8] M. S. Grady, M. A. Howard, J. A. Molloy, R. C. Ritter, E. G. Quate, and G. T. Gillies, Med. Phys. **17**, 405 (1990).

[9] J.-B. Mathieu, G. Beaudoin, and S. Martel, IEEE Trans. Biomed. Eng. **53**, 292 (2006).

[10] E. B. Steager, M. S. Sakar, D. H. Kim, V. Kumar, G. J. Pappas, and M. J. Kim, J. Micromech. Microeng. **21**, 035001 (2011).

[11] D. H. Kim, U. K. Cheang, L. Kőhidai, D. Byun, M. J. Kim *et al.*, Appl. Phys. Lett. **97**, 173702 (2010).

[12] M. Leoni, J. Kotar, B. Bassetti, P. Cicuta, and M. C. Lagomarsino, Soft Matter **5**, 472 (2009).

[13] N. Mori, K. Kuribayashi, and S. Takeuchi, Appl. Phys. Lett. **96**, 083701 (2010).

[14] R. F. Ismagilov, A. Schwartz, N. Bowden, and G. M. Whitesides, Angew. Chem. **114**, 674 (2002).

[15] W. F. Paxton, K. C. Kistler, C. C. Olmeda, A. Sen, S. K. St. Angelo, Y. Cao, T. E. Mallouk, P. E. Lammert, and V. H. Crespi, J. Am. Chem. Soc. **126**, 13424 (2004).

[16] Y. Wang, R. M. Hernandez, D. J. Bartlett, J. M. Bingham, T. R. Kline, A. Sen, and T. E. Mallouk, Langmuir **22**, 10451 (2006).

[17] W. Gao, M. D'Agostino, V. Garcia-Gradilla, J. Orozco, and J. Wang, Small **9**, 467 (2013).

[18] J. Orozco, V. García-Gradilla, M. DAgostino, W. Gao, A. Corte, and J. Wang, ACS Nano **7**, 818 (2013).

[19] K. M. Manesh, M. Cardona, R. Yuan, M. Clark, D. Kagan, S. Balasubramanian, and J. Wang, ACS Nano **4**, 1799 (2010).

[20] A. A. Solovev, Y. Mei, E. Bermúdez Ureña, G. Huang, and O. G. Schmidt, Small **5**, 1688 (2009).

[21] J. Gibbs and Y.-P. Zhao, Appl. Phys. Lett. **94**, 163104 (2009).

[22] T. R. Kline, W. F. Paxton, T. E. Mallouk, and A. Sen, Angew. Chem. **117**, 754 (2005).

[23] C. E. Sing, L. Schmid, M. F. Schneider, T. Franke, and A. Alexander-Katz, Proc. Natl. Acad. Sci. USA **107**, 535 (2010).

[24] P. Tierno, O. Güell, F. Sagués, R. Golestanian, and I. Pagonabarraga, Phys. Rev. E **81**, 011402 (2010).

[25] L. Zhang, T. Petit, Y. Lu, B. E. Kratochvil, K. E. Peyer, R. Pei, J. Lou, and B. J. Nelson, ACS Nano **4**, 6228 (2010).

[26] W. Xi, A. A. Solovev, A. N. Ananth, D. H. Gracias, S. Sanchez, and O. G. Schmidt, Nanoscale **5**, 1294 (2013).

[27] E. M. Purcell, Am. J. Phys **45**, 3 (1977).

[28] Z. Vaituzis and R. Doetsch, J. Bacteriol. **100**, 512 (1969).

[29] L. Zhang, E. Ruh, D. Grützmacher, L. Dong, D. J. Bell, B. J. Nelson, and C. Schönenberger, Nano Lett. **6**, 1311 (2006).

[30] S. Tottori, L. Zhang, F. Qiu, K. K. Krawczyk, A. Franco-Obregón, and B. J. Nelson, Adv. Mater. **24**, 811 (2012).

[31] A. Ghosh and P. Fischer, Nano Lett. **9**, 2243 (2009).

[32] U. K. Cheang, D. Roy, J. H. Lee, and M. J. Kim, Appl. Phys. Lett. **97**, 213704 (2010).

[33] F. Z. Temel and S. Yesilyurt, in *Mechatronics (ICM), 2011 IEEE International Conference on* (IEEE, New York, 2011), pp. 342–347.

[34] P. Garstecki, P. Tierno, D. B. Weibel, F. Sagués, and G. M. Whitesides, J. Phys. Condens. Matter **21**, 204110 (2009).

[35] L. Zhang, J. J. Abbott, L. Dong, B. E. Kratochvil, D. Bell, and B. J. Nelson, Appl. Phys. Lett. **94**, 064107 (2009).

[36] R. Dreyfus, J. Baudry, M. L. Roper, M. Fermigier, H. A. Stone, and J. Bibette, Nature (London) **437**, 862 (2005).

[37] W. Gao, D. Kagan, O. S. Pak, C. Clawson, S. Campuzano, E. Chuluun-Erdene, E. Shipton, E. E. Fullerton, L. Zhang, E. Lauga *et al.*, Small **8**, 460 (2012).

[38] O. S. Pak, W. Gao, J. Wang, and E. Lauga, Soft Matter **7**, 8169 (2011).

[39] E. P. Diamandis and T. K. Christopoulos, Clin. Chem. **37**, 625 (1991).

[40] J. Wong, A. Chilkoti, and V. T. Moy, Biomol. Eng. **16**, 45 (1999).

[41] K. K.-W. Lo, W.-K. Hui, C.-K. Chung, K. H.-K. Tsang, T. K.-M. Lee, and D. C.-M. Ng, J. Chin. Chem. Soc. **53**, 53 (2006).

[42] See Supplemental Material at http://link.aps.org/supplemental/10.1103/PhysRevE.90.033007 for videos of flexibility tests, controlled trajectory, and changing rotation axis.

[43] K. E. Peyer, L. Zhang, B. E. Kratochvil, and B. J. Nelson, *2010 IEEE International Conference on Robotics and Automation*, 96 (IEEE, New York, 2010).
[44] Y. Sun, S. Duthaler, and B. J. Nelson, Microsc. Res. Technique **65**, 139 (2004).
[45] H. C. Berg, *Random Walks in Biology* (Princeton University Press, Princeton, 1993).
[46] J. Happel and H. Brenner, *Low Reynolds Number Hydrodynamics: with Special Applications to Particulate Media*, Vol. 1 (Springer, Berlin, 1983).
[47] Y. Hyon, T. R. Powers, R. Stocker, H. C. Fu *et al.*, J. Fluid Mech. **705**, 58 (2012).
[48] Note that this form of nonzero **C** is also consistent with the example of the achiral impeller given by Happel and Brenner.
[49] R. Cortez, SIAM J. Sci. Comput. **23**, 1204 (2001).
[50] R. Cortez, L. Fauci, and A. Medovikov, Phys. Fluid. **17**, 031504 (2005).
[51] P. Dhar, C. D. Swayne, T. M. Fischer, T. Kline, and A. Sen, Nano Lett. **7**, 1010 (2007).
[52] A. Ghosh, D. Paria, H. J. Singh, P. L. Venugopalan, and A. Ghosh, Phys. Rev. E **86**, 031401 (2012).
[53] Y. Man and E. Lauga, Phys. Fluid. **25**, 071904 (2013).